

HAT-P-47b AND HAT-P-48b: TWO LOW DENSITY SUB-SATURN-MASS TRANSITING PLANETS ON THE EDGE OF THE PERIOD–MASS DESERT[†]

G. Á. BAKOS^{1,†}, J. D. HARTMAN¹, G. TORRES², D. W. LATHAM², B. SATO³, A. BIERYLA², A. SHPORER^{4,5},
A. W. HOWARD⁶, B. J. FULTON^{6,14}, L. A. BUCHHAVE⁷, K. PENEV¹, G. KOVÁCS⁸, T. KOVÁCS⁸, Z. CSUBRY¹,
G. A. ESQUERDO³, M. EVERETT⁹, T. SZKLENÁR¹², S. N. QUINN¹³, B. BÉKY¹⁰, G. W. MARCY¹¹, R. W. NOYES²,
J. LÁZÁR¹², I. PAPP¹², P. SÁRI¹²

Draft version June 16, 2016

ABSTRACT

We report the discovery of two new transiting extrasolar planets orbiting moderately bright ($V = 10.7$ and 12.2 mag) F stars (masses of $1.39 M_{\odot}$ and $1.10 M_{\odot}$, respectively). The planets have periods of $P = 4.7322$ d and 4.4087 d, and masses of $0.21 M_J$ and $0.17 M_J$ which are almost half-way between those of Neptune and Saturn. With radii of $1.31 R_J$ and $1.13 R_J$, these very low density planets are the two lowest mass planets with radii in excess that of Jupiter. Comparing with other recent planet discoveries, we find that sub-Saturns ($0.18 M_J < M_p < 0.3 M_J$) and super-Neptunes ($0.05 M_J < M_p \leq 0.18 M_J$) exhibit a wide range of radii, and their radii exhibit a weaker correlation with irradiation than higher mass planets. The two planets are both suitable for measuring the Rossiter-McLaughlin effect and for atmospheric characterization. Measuring the former effect would allow an interesting test of the theory that star–planet tidal interactions are responsible for the tendency of close-in giant planets around convective envelope stars to be on low obliquity orbits. Both planets fall on the edge of the short period Neptunian desert in the semi-major axis–mass plane.

Subject headings: planetary systems — stars: individual (HAT-P-47, GSC 2324-00031, HAT-P-48, GSC 2326-00214) — techniques: spectroscopic, photometric

1. INTRODUCTION

One of the startling discoveries in the field of exoplanets is that at fixed mass planets show a very wide spread in radii (and bulk density). For example, within the narrow mass range of $0.85 M_J$ to $0.9 M_J$, planets have been found with radii ranging from $0.78 R_J$ (WASP-59b; Hébrard et al. 2013) up to $2.1 R_J$ (WASP-79b; Smalley et al. 2012). While some variance is expected due to differences in composition, age, and irradiation (e.g., Burrows et al. 2007), explaining the very large radius planets remains a puzzle (Spiegel & Burrows 2013). Observationally the radii of giant planets have been found to correlate tightly with the degree of stellar irradiation, with more highly irradiated planets having larger radii (Kovács et al. 2010). While it is unclear to what extent selection effects are responsible for this correlation, most theoretical models do predict larger radii with increased irradiation.

There is some evidence that the influence of irradiation on the planetary radii depends on planetary mass, with super-Jupiters spanning a smaller range of radii than sub-Jupiters (e.g., Huang et al. 2015). On the other hand, planet mass and radius are essentially uncorrelated for planets with masses greater than Saturn. Below Saturn-mass the radii are observed to decrease, with all planets discovered to date below the mass of Neptune having radii less than $0.85 R_J$, excluding the Kepler-51 system (Masuda 2014) which has unusually bloated planets (with large uncertainties on their masses). However, due to the small number of low-mass transiting planets with precisely measured masses and radii, it has been difficult to draw firm conclusions about the spread in the mass–radius relation below the mass of Saturn or the influence of other parameters such as irradiation or

¹ Department of Astrophysical Sciences, Princeton University, Princeton, NJ 08544; email: gbakos@astro.princeton.edu

[†] Packard Fellow

² Harvard-Smithsonian Center for Astrophysics, Cambridge, MA

³ Department of Earth and Planetary Sciences, Tokyo Institute of Technology, 2-12-1 Ookayama, Meguro-ku, Tokyo 152-8551

⁴ Jet Propulsion Laboratory, California Institute of Technology, 4800 Oak Grove Drive, Pasadena, CA 91109, USA

⁵ NASA Sagan Fellow

⁶ Institute for Astronomy, University of Hawaii, 2680 Woodlawn Drive, Honolulu, HI 96822

⁷ Niels Bohr Institute, University of Copenhagen, DK-2100, Denmark, and Centre for Star and Planet Formation, Natural History Museum of Denmark, DK-1350 Copenhagen

^{8,15} Konkoly Observatory of the Hungarian Academy of Sciences, Budapest, Hungary

⁹ Steward Observatory, University of Arizona, Tucson, AZ

¹⁰ Google

¹¹ Department of Astronomy, University of California, Berkeley, CA

¹² Hungarian Astronomical Association, Budapest, Hungary

¹³ Department of Physics and Astronomy, Georgia State University, Atlanta, GA

¹⁴ NSF Graduate Research Fellow

¹⁵ Institute of Theoretical Physics, Eötvös University, H-1117 Budapest, Hungary

[†] Based in part on observations obtained at the W. M. Keck Observatory, which is operated by the University of California and the California Institute of Technology. Keck time has been granted by NOAO (A284Hr, A245Hr) and NASA (N108Hr, N154Hr, N130Hr). Based in part on data collected at Subaru Telescope (program o11170), which is operated by the National Astronomical Observatory of Japan. Based in part on observations made with the Nordic Optical Telescope, operated on the island of La Palma jointly by Denmark, Finland, Iceland, Norway, and Sweden, in the Spanish Observatorio del Roque de los Muchachos of the Instituto de Astrofísica de Canarias. Based in part on observations obtained with facilities of the Las Cumbres Observatory Global Telescope.

metallicity on this relation.

In this paper we present the discovery and characterization of two new low-mass transiting planets by the HATNet project (Bakos et al. 2004), called HAT-P-47b and HAT-P-48b. In Section 2 we summarize the detection of the photometric transit signal and the subsequent spectroscopic and photometric observations of each star to confirm the planets. In Section 3 we analyze the data to rule out false positive scenarios, and to determine the stellar and planetary parameters. Our findings are briefly discussed in Section 4.

2. OBSERVATIONS

HAT-P-47b and HAT-P-48b were discovered through a combination of photometric and spectroscopic observations. See previous HATNet transiting exoplanet (TEP) discovery papers for a general description of the method (e.g. Bakos et al. 2010; Latham et al. 2009). Below we summarize the observations that led to the two discoveries presented here. Identifying information for these stars is provided later in the paper (Table 7).

2.1. Photometric detection

Table 1 summarizes the photometric observations that we performed of HAT-P-47 and HAT-P-48. These include discovery light curves obtained with the fully automated HATNet system, which were generated and filtered for noise following Bakos et al. (2010). These light curves were searched for periodic transit signals using the Box Least-Squares (BLS; see Kovács et al. 2002) method, leading to the identification of HAT-P-47 and HAT-P-48 as candidate TEP systems (Figure 1) with the following properties:

- *HAT-P-47* – GSC 2324-00031 (also known as 2MASS 02331396+3021377; $\alpha = 02^{\text{h}}33^{\text{m}}13.97\text{s}$, $\delta = +30^{\circ}21'37.8''$; J2000; $V = 10.694 \pm 0.063$, Droege et al. 2006). A signal was detected for this star with an apparent depth of ~ 3.8 mmag, and a period of $P = 4.7322$ days. Discrete Fourier Transformation (DFT) frequency spectrum did not detect any component in excess of 0.5 mmag amplitude in the [0,50] cycles/day frequency range. No significant second frequency peak was seen in the BLS spectrum.
- *HAT-P-48* – GSC 2326-00214 (also known as 2MASS 02575301+3037324; $\alpha = 02^{\text{h}}57^{\text{m}}53.03\text{s}$, $\delta = +30^{\circ}37'32.5''$; J2000; $V = 12.16 \pm 0.11$, Droege et al. 2006). A signal was detected for this star with an apparent depth of ~ 6.4 mmag, and a period of $P = 4.4087$ days. The DFT frequency spectrum showed no significant peak in excess of 0.6 mmag in the range of [0,50] cycles/day.

2.2. Reconnaissance Spectroscopy

High-resolution, low-S/N “reconnaissance” spectra were obtained for HAT-P-47 and HAT-P-48 using the Tillinghast Reflector Echelle Spectrograph (TRES; Fúresz 2008) on the 1.5 m Tillinghast Reflector at the Fred Lawrence Whipple Observatory (FLWO) in AZ. The reconnaissance spectroscopic observations and results for each system are summarized in Table 2.

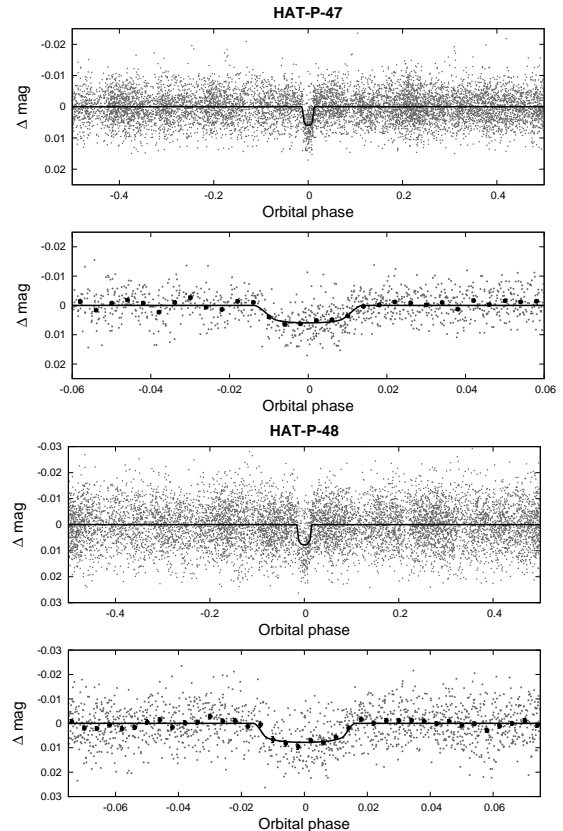


FIG. 1.— HATNet light curves of HAT-P-47 (top) and HAT-P-48 (bottom) phase folded with the transit period. In each case we show two panels: the top shows the unbinned light curve, while the bottom shows the region zoomed-in on the transit, with dark filled circles for the light curve binned in phase with a binsize of 0.004. The solid line shows the model fit to the light curve.

The observations were reduced and analyzed following the procedure described by Quinn et al. (2012) and Buchhave et al. (2010).

Based on the observations summarized in Table 2 we find that both targets are dwarf stars with radial velocity (RV) root mean square (rms) residuals consistent with no detectable RV variation within the $\lesssim 200 \text{ m s}^{-1}$ precision of the measurements. All spectra were single-lined, i.e., there is no evidence that any of these targets consist of more than one star.

2.3. High resolution, high S/N spectroscopy

We proceeded with the follow-up of each candidate by obtaining high-resolution, high-S/N spectra to characterize the RV variations, and to refine the determination of the stellar parameters. The observations were made with HIRES (Vogt et al. 1994) on the Keck-I telescope in Hawaii, with FIES on the Nordic Optical Telescope on the island of La Palma, Spain (Djupvik & Andersen 2010), and with the High-Dispersion Spectrograph (HDS; Noguchi et al. 2002) on the 8.2 m Subaru telescope in Hawaii. For HIRES and HDS we used an I₂ absorption cell, while for FIES we relied on simultaneous ThAr spectra to determine the wavelength correction. All but one of the HIRES observations were obtained with the C2 decker which provides a resolution of $R = 45,000$, with the remaining observation made with the B5 decker on the night of 01 Sep 2011. This latter decker provides

TABLE 1
SUMMARY OF PHOTOMETRIC OBSERVATIONS

Instrument/Field	Date(s)	Number of Images	Mode	Cadence (min)	Filter
HAT-P-47					
HAT-5/G212	2010 Sep–2010 Nov	2200		5.5	Sloan <i>r</i> band
HAT-8/G212	2010 Aug–2010 Nov	6000		3.5	Sloan <i>r</i> band
KeplerCam	2010 Dec 26	137		1.2	Sloan <i>i</i> band
KeplerCam	2011 Jan 09	466		0.7	Sloan <i>i</i> band
BOS	2011 Aug 24	94		1.7	Sloan <i>i</i> band
BOS	2011 Oct 01	307		0.7	Sloan <i>i</i> band
FTN	2011 Oct 15	266		0.7	Sloan <i>i</i> band
FTN	2012 Jan 13	345		0.6	Sloan <i>i</i> band
HAT-P-48					
HAT-5/G212	2010 Sep–2010 Nov	2200		5.5	Sloan <i>r</i> band
HAT-8/G212	2010 Aug–2010 Nov	6000		3.5	Sloan <i>r</i> band
KeplerCam	2011 Jan 12	328		0.9	Sloan <i>i</i> band
KeplerCam	2011 Sep 20	231		0.9	Sloan <i>i</i> band
KeplerCam	2011 Oct 30	137		1.5	Sloan <i>i</i> band
KeplerCam	2011 Nov 21	201		1.5	Sloan <i>i</i> band
FTN	2012 Jan 26	99		1.1	Sloan <i>i</i> band

TABLE 2
SUMMARY OF RECONNAISSANCE SPECTROSCOPY OBSERVATIONS.

Instrument	$HJD - 2400000$	$T_{\text{eff}\star}$ (K)	$\log g_{\star}$ (cgs)	$v \sin i$ (km s^{-1})	$\gamma_{\text{RV}}^{\text{a}}$ (km s^{-1})
HAT-P-47					
TRES	55544.64583	6700	4.1	14	2.72
TRES	55546.65187	6650	4.2	14	2.69
HAT-P-48					
TRES	55546.76439	5850 ± 50	4.15 ± 0.10	3.0 ± 0.5	18.31
TRES	55549.69608	6050 ± 100	4.53 ± 0.18	4.0 ± 0.8	18.26

^a The heliocentric RV of the target on the IAU system, with a systematic uncertainty of approximately 0.1 km s^{-1} mostly limited by how well the velocities of the standard stars have been established.

the same resolution as C2, but with a shorter slit length. For the FIES observations we used the high-resolution fiber yielding a spectral resolution of $R = 67,000$, while for HDS we used the $0''.6 \times 2''.0$ slit yielding a spectral resolution of $R = 60,000$. The HIRES observations were reduced to radial velocities in the barycentric frame following the procedure described by Butler et al. (1996); the FIES observations were reduced following Buchhave et al. (2010); and the HDS observations were reduced following Sato et al. (2002, 2012). The RV measurements and uncertainties are given in Tables 3 and 4 for HAT-P-47 and HAT-P-48, respectively. The period-folded data, along with our best fit described below in Section 3 are displayed in Figures 2 and 3.

In each figure we show also the spectral line bisector spans (BSs) computed from the Keck/HIRES spectra following Torres et al. (2007) and the S activity index calculated following Isaacson & Fischer (2010).

2.4. Photometric follow-up observations

We conducted additional photometric observations of both stars with the KeplerCam CCD camera on the FLWO 1.2m telescope. For HAT-P-47 we also made use of the Spectral CCD on the 2.0m Faulkes Telescope North (FTN) at Haleakala Observatory in Hawaii, and

the SBIG CCD imager on the Byrne Observatory at Sedgwick (BOS) 0.8m telescope, at Sedgwick Reserve in the Santa Ynez Valley, CA. Both FTN and BOS are operated by the Las Cumbres Observatory Global Telescope¹⁸ (Brown et al. 2013). The observations for each target are summarized in Table 1.

The reduction of the KeplerCam images to light curves was performed as described by Bakos et al. (2010). The FTN and BOS images were reduced in a similar manner. We performed external parameter decorrelation (EPD) and the trend filtering algorithm (TFA) to remove trends simultaneously with the light curve modeling (for more details, see Bakos et al. (2010)). The final time series, together with our best-fit transit light curve model, are shown in the top portion of Figures 4 and 5, while the individual measurements are reported in Tables 5 and 6. All relevant data (discovery, follow-up), just like for other HATNet discoveries, are also reported at the HATNet website¹⁹.

3. ANALYSIS

3.1. Excluding blend scenarios

¹⁸ <http://lcogt.net>

¹⁹ www.hatnet.org

TABLE 3
RELATIVE RADIAL VELOCITIES, BISECTOR SPANS, AND ACTIVITY INDEX MEASUREMENTS
OF HAT-P-47.

BJD ^a (2,454,000+)	RV ^b (m s ⁻¹)	σ_{RV} ^c (m s ⁻¹)	BS (m s ⁻¹)	σ_{BS} (m s ⁻¹)	S ^d	Phase	Instrument
1557.93452	-30.59	7.79	2.88	21.90	0.142	0.086	Keck
1584.81706	-14.87	16.53	0.145	0.767	Keck
1584.86677	55.12	6.30	-6.73	21.22	0.144	0.777	Keck
1611.80587	16.32	6.83	4.59	35.18	0.146	0.470	Keck
1634.73217	18.92	6.11	26.23	35.18	0.145	0.315	Keck
1780.10010	-17.66	16.40	0.034	Subaru
1780.10439	-4.03	19.70	0.034	Subaru
1781.10948	14.07	17.07	0.247	Subaru
1781.11548	-31.26	9.77	0.248	Subaru
1781.12325	-14.12	13.00	0.250	Subaru
1782.08387	-16.86	13.77	0.453	Subaru
1782.09162	-8.30	15.18	0.454	Subaru
1782.09938	6.14	16.01	0.456	Subaru
1783.12240	19.51	6.59	11.42	14.82	0.144	0.672	Keck
1783.13154	21.88	12.45	0.674	Subaru
1790.12677	-41.16	5.91	10.85	10.75	0.147	0.152	Keck
1791.12635	-37.32	7.00	-2.77	8.06	0.146	0.364	Keck
1796.11735	-35.04	7.99	-10.40	13.96	0.146	0.418	Keck
1807.12575	21.94	7.18	24.75	34.07	0.146	0.745	Keck
1812.08066	5.64	5.37	-12.56	6.83	0.146	0.792	Keck
1815.03365	-23.62	5.93	-18.32	10.50	0.147	0.416	Keck
1853.83582	-2.77	7.24	19.24	10.87	0.144	0.615	Keck
1870.96307	-48.27	6.35	4.26	10.85	0.137	0.235	Keck
1878.88618	7.84	6.01	18.88	14.82	0.142	0.909	Keck
1879.88871	9.83	6.88	32.28	14.30	0.141	0.121	Keck
1880.98816	14.96	5.95	19.38	11.22	0.144	0.353	Keck
1882.07816	43.69	10.01	-42.58	18.76	0.133	0.583	Keck
1944.76249	4.30	6.31	-9.98	11.80	0.144	0.830	Keck
1960.83339	-10.87	6.86	-15.44	17.99	0.139	0.226	Keck
1972.82552	28.68	4.82	6.52	11.75	0.139	0.760	Keck
1996.77476	-34.83	13.60	-1.69	31.67	0.121	0.821	Keck
2138.06092	18.43	7.48	0.146	0.678	Keck

NOTE. — Note that for the iodine-free Keck/HIRES template exposures we do not measure the RV but do measure the BS and S index. Such template exposures can be distinguished by the missing RV value. For the Subaru iodine-free template we did not measure the BS and S index (consequently, it is missing from the table). We exclude BS measurements for a handful of measurements which were heavily affected by contamination from scattered moonlight.

^a Barycentric Julian Date calculated directly from UTC, *without* correction for leap seconds.

^b The zero-point of these velocities is arbitrary. An overall offset γ_{rel} fitted independently to the velocities for each instrument has been subtracted.

^c Internal errors excluding the component of astrophysical jitter considered in Section 3.2.

^d Chromospheric activity index.

The analyses of our reconnaissance spectroscopic observations discussed in Section 2.2 rule out many of the astrophysical false positive scenarios for HAT-P-47 and HAT-P-48. To rule out remaining scenarios we conduct an analysis similar to that done in Hartman et al. (2011, 2012). This involves modeling the available light curves, absolute photometry, and stellar atmospheric parameters as a combination of three stars (either a hierarchical triple, or an unresolved blend between a foreground star and a background eclipsing binary system) using the Padova isochrones (Girardi et al. 2002) to constrain the properties of the stars in the simulated systems. For each simulation we also predict the RVs and BS values that would have been measured with Keck/HIRES at the times of observation, and we compare them with the actual observations.

We find that for HAT-P-47 the photometry and measured stellar atmospheric parameters rule out hierarchical triple eclipsing stellar binary systems with the more massive of the eclipsing stars having $M < 0.89 M_{\odot}$, or blended eclipsing binary systems where the background eclipsing binary has a distance modulus that is more than

2.25 mag larger than the distance modulus to the foreground star. In both cases these are 5σ limits based on Monte Carlo simulations which allow for the possibility of time-correlated noise in the photometry. We also find that the simulated RV and BS measurements exclude hierarchical triple systems where the more massive of the eclipsing stars has $M > 0.69 M_{\odot}$, or blended systems where the difference in distance moduli is less than 3.35 mag. Systems excluded by these limits would show RV and/or BS scatter (RMS) that is at least 5 times greater than what was observed. Combining these constraints we conclude that HAT-P-47 cannot be a hierarchical triple eclipsing stellar binary system, or a blend between a foreground star and a background eclipsing binary.

The analysis for HAT-P-48 yields a similar result. Here the photometry rules out hierarchical triples with the more massive of the eclipsing stars having $M < 0.88 M_{\odot}$ or blended eclipsing binary systems with distance moduli differences > 1 mag, while the simulated RV and BS measurements exclude hierarchical triples with $M > 0.69 M_{\odot}$, or blended eclipsing binary systems with dis-

TABLE 4
RELATIVE RADIAL VELOCITIES, BISECTOR SPANS, AND ACTIVITY INDEX MEASUREMENTS
OF HAT-P-48.

BJD ^a (2,454,000+)	RV ^b (m s ⁻¹)	σ_{RV} ^c (m s ⁻¹)	BS (m s ⁻¹)	σ_{BS} (m s ⁻¹)	S ^d	Phase	Instrument
1557.94958	-37.91	5.66	-31.23	11.12	0.122	0.203	Keck
1584.83402	15.76	9.32	0.135	0.301	Keck
1584.85683	-18.72	4.16	-19.17	24.21	0.137	0.306	Keck
1611.83497	-4.56	5.27	46.93	12.76	0.126	0.425	Keck
1634.74237	43.01	4.92	15.71	32.57	0.141	0.621	Keck
1779.68487	21.90	9.20	0.498	FIES
1780.07705	16.14	9.54	-9.11	23.26	...	0.587	Subaru
1780.08485	14.42	8.61	6.75	21.41	...	0.589	Subaru
1780.09261	-4.77	10.40	10.18	21.93	...	0.591	Subaru
1780.70889	11.50	9.40	0.730	FIES
1781.05224	22.34	9.27	-3.01	22.96	...	0.808	Subaru
1781.06001	28.26	7.48	5.59	22.00	...	0.810	Subaru
1781.06778	15.23	7.31	7.32	21.53	...	0.812	Subaru
1781.08022	-2.25	21.00	...	0.815	Subaru
1781.09494	6.19	26.40	...	0.818	Subaru
1781.69965	-11.80	8.00	0.955	FIES
1782.05225	-18.74	12.80	4.20	23.72	...	0.035	Subaru
1782.06002	0.11	10.76	-14.68	24.22	...	0.037	Subaru
1782.07119	-13.29	7.84	4.39	24.52	...	0.039	Subaru
1783.09288	-20.51	11.55	0.85	23.79	...	0.271	Subaru
1783.10066	-9.15	8.94	-11.30	24.06	...	0.273	Subaru
1783.11016	-10.90	8.80	0.01	20.35	...	0.275	Subaru
1815.04453	-24.25	4.12	-20.78	8.20	0.145	0.519	Keck
1853.84571	-3.11	4.22	32.51	9.70	0.136	0.320	Keck
1857.57640	-29.20	12.30	0.166	FIES
1858.63379	15.50	12.10	0.406	FIES
1859.65351	6.90	8.00	0.637	FIES
1877.94245	37.27	4.28	-100.83	36.09	0.139	0.785	Keck
1882.10175	-8.16	4.99	-131.16	58.69	0.122	0.729	Keck
1944.81352	12.26	4.61	-10.28	9.25	0.136	0.954	Keck
1964.77835	-14.35	8.57	4.29	22.52	...	0.482	Subaru
1964.78611	-4.14	9.71	-12.71	24.55	...	0.484	Subaru
1964.79387	3.39	9.95	-16.91	21.30	...	0.486	Subaru
1967.81621	-8.31	11.72	-1.74	25.87	...	0.171	Subaru
1967.83092	-21.10	10.71	10.02	19.76	...	0.175	Subaru
1967.84563	-28.85	11.18	11.92	24.22	...	0.178	Subaru

NOTE. — Note that for the iodine-free Keck/HIRES template exposures we do not measure the RV but do measure the BS as well as the S index (in the case of HIRES). Such template exposures for HIRES and HDS can be distinguished by the missing RV value.

^a Barycentric Julian Date calculated directly from UTC, *without* correction for leap seconds.

^b The zero-point of these velocities is arbitrary. An overall offset γ_{rel} fitted independently to the velocities for each instrument has been subtracted.

^c Internal errors excluding the component of astrophysical jitter considered in Section 3.2.

^d Chromospheric activity index.

tance moduli differences < 2.35 mag. As for HAT-P-47 we conclude that HAT-P-48 cannot be a hierarchical triple eclipsing stellar binary system, or a blend between a foreground star and a background eclipsing binary.

While we exclude the possibility that either object is solely a combination of stellar mass components, we cannot rule out the possibility that either system is a combination of two stars (physically associated, or aligned on the sky by chance), one of which hosts a planet. However, given the absence of evidence that either object is composed of more than one star, we proceed by analyzing both objects as single stars orbited by transiting planets.

3.2. Global modeling of the data

We analyzed both systems following the procedure of Bakos et al. (2010) as amended by Hartman et al. (2012). To summarize: (1) we determine stellar atmospheric parameters for each star by applying the Stellar Parameter Classification method (Buchhave et al. 2012) to the Keck/HIRES iodine-free template spectra; (2) we

then conduct a Markov-Chain Monte Carlo (MCMC)-based modeling of the available light curves and RVs, which, among others, results in a posterior distribution for the mean stellar density. We fix the limb darkening coefficients to values taken from Claret (2004) for the measured atmospheric parameters; (3) we use the effective temperatures and metallicities of the stars measured from the spectra, together with the above determined stellar densities to derive the stellar properties based on the Yonsei-Yale (YY) theoretical stellar evolution models (Yi et al. 2001). The stellar properties so-determined include the masses, radii and ages. We also determine the planetary parameters (e.g. mass and radius) which depend on these values; (4) we re-analyze the Keck/HIRES spectra fixing the stellar surface gravities to the values found in (3), and we go back to steps (2) and (3).

For both systems we conducted the analysis twice: fixing the eccentricity to zero, and allowing it to vary. For each system we find that the eccentricity is consistent with zero, but with a poor constraint (the 95% upper

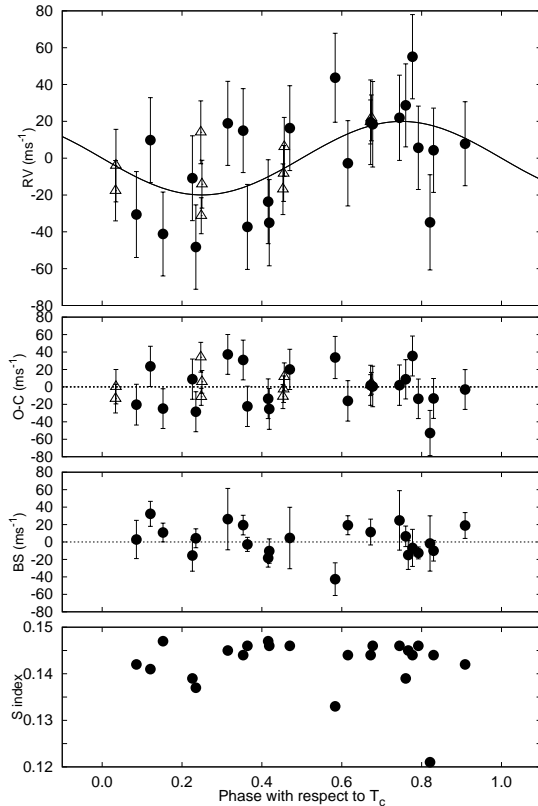


FIG. 2.— *Top panel:* RV measurements from Keck/HIRES (filled circles) and Subaru/HDS (open triangles) for HAT-P-47 shown as a function of orbital phase, along with our best-fit circular model (solid line; see Table 9), and our best-fit eccentric model (dashed line). Zero phase corresponds to the time of mid-transit. The center-of-mass velocity has been subtracted. *Second panel:* Velocity $O-C$ residuals from the best fit. The error bars for Keck/HIRES include a component from astrophysical jitter (22.0 m s^{-1}) added in quadrature to the formal errors (see Section 3.2). *Third panel:* Bisector spans (BS), with the mean value subtracted. The measurement from the template spectrum is included. The BS uncertainties are internal errors determined for each spectrum from the scatter of the individual BS values measured on separate orders of the spectrum; they do not include the unknown contribution from stellar jitter. *Bottom panel:* Chromospheric activity index S .

limits on the eccentricity are $e < 0.31$ for HAT-P-47b and $e < 0.46$ for HAT-P-48b). Following Anderson et al. (2012) we adopt the parameter values associated with the fixed circular orbits. The adopted stellar parameters are given in Table 7 while the adopted planetary parameters are given in Table 9. We find that HAT-P-47 is a $1.387 \pm 0.038 M_{\odot}$ mass star with a radius of $1.515 \pm 0.040 R_{\odot}$, and is located at a reddening-corrected distance of $268 \pm 7 \text{ pc}$, while HAT-P-48 is a $1.099 \pm 0.041 M_{\odot}$ mass star with a radius of $1.223 \pm 0.046 R_{\odot}$, and is located at a reddening-corrected distance of $305 \pm 12 \text{ pc}$. The respective planets have masses of $0.206 \pm 0.039 M_{\text{J}}$ and $0.168 \pm 0.024 M_{\text{J}}$, and radii of $1.313 \pm 0.045 R_{\text{J}}$ and $1.131 \pm 0.054 R_{\text{J}}$. The parameters which result when the eccentricities are allowed to vary are listed in Tables 8 and 10.

4. DISCUSSION

We show the location of HAT-P-47b and HAT-P-48b on a mass–radius diagram in Fig. 6. In this same Figure we show and label other transiting exoplanets with $M_p < 0.3 M_{\text{J}}$ (sub-Saturn mass), and with masses having relative error $\delta(M_p) < 20\%$. The values are taken

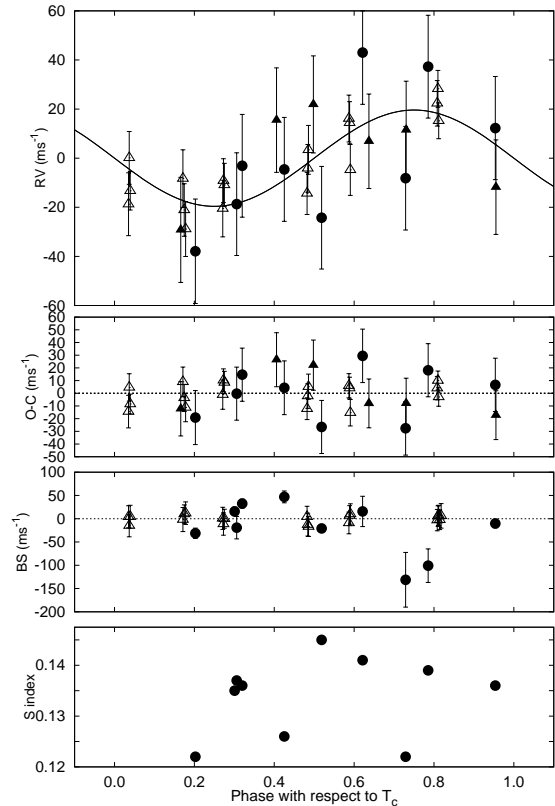


FIG. 3.— Keck/HIRES, Subaru/HDS, and NOT/FIES observations of HAT-P-48. The panels are as in Figure 2. Here we use filled circles to show Keck/HIRES observations, open triangles to show Subaru/HDS observations, and filled triangles to show NOT/FIES observations. BS measurements are only available for the Keck/HIRES and Subaru/HDS observations, while S index measurements are only available for the Keck/HIRES observations. The parameters used in the best-fit model are given in Table 9.

TABLE 5
HIGH-PRECISION DIFFERENTIAL PHOTOMETRY OF HAT-P-47.

BJD ^a (2,400,000+)	Mag ^b	σ_{Mag}	Mag(orig) ^c	Filter
55557.57382	0.00470	0.00053	9.53342	<i>i</i>
55557.57467	0.00503	0.00053	9.53342	<i>i</i>
55557.57553	0.00555	0.00054	9.53607	<i>i</i>
55557.57639	0.00541	0.00051	9.53445	<i>i</i>
55557.57724	0.00570	0.00050	9.53334	<i>i</i>
55557.57810	0.00465	0.00049	9.53297	<i>i</i>
55557.57895	0.00446	0.00049	9.53267	<i>i</i>
55557.57979	0.00314	0.00049	9.53163	<i>i</i>
55557.58065	0.00211	0.00049	9.53065	<i>i</i>
55557.58148	0.00207	0.00049	9.53096	<i>i</i>

NOTE. — This table is available in a machine-readable form in the online journal. A portion is shown here for guidance regarding its form and content.

^a Barycentric Julian Date calculated directly from UTC, *without* correction for leap seconds.

^b The out-of-transit level has been subtracted. These magnitudes have been subjected to the EPD and TFA procedures, carried out simultaneously with the transit fit.

^c Raw magnitude values without application of the EPD and TFA procedures.

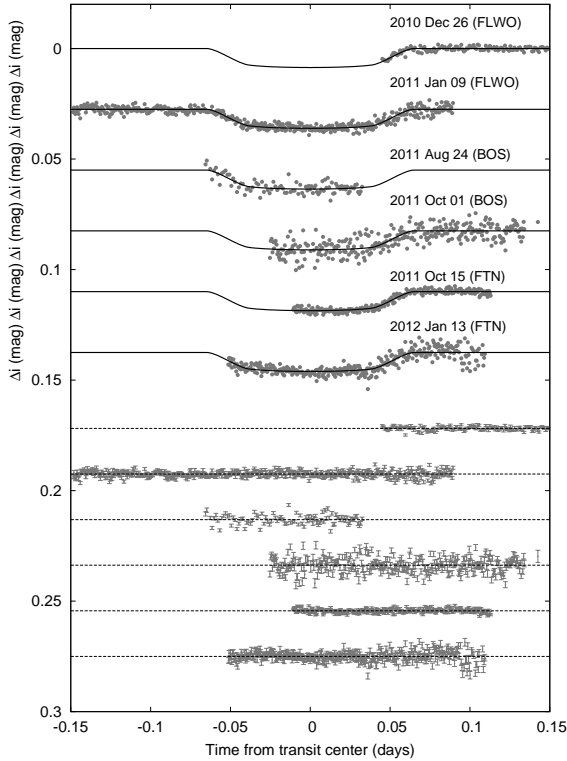


FIG. 4.— Unbinned transit light curves for HAT-P-47, acquired with KeplerCam at the FLWO 1.2 m telescope. The light curves have been EPD- and TFA-processed, as described in § 3.2. The dates of the events are indicated. Curves after the first are displaced vertically for clarity. Our best fit from the global modeling described in Section 3.2 is shown by the solid lines. Residuals from the fits are displayed at the bottom, in the same order as the top curves. The error bars represent the photon and background shot noise, plus the readout noise.

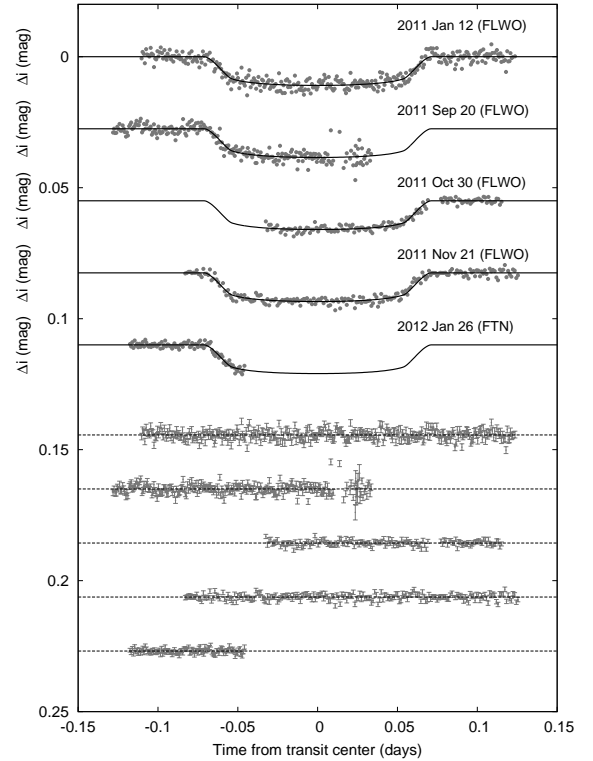


FIG. 5.— Similar to Figure 4; here we show the follow-up light curves for HAT-P-48. The facility used for each each light curve is indicated next to the date of the event.

from our privately maintained database of up-to-date exoplanet parameters, which is broadly consistent with the NASA exoplanet archive²⁰. HAT-P-47b and HAT-P-48b are the two lowest density sub-Saturn planets, and they are the two lowest mass planets discovered to date with radii larger than Jupiter. If all planets are considered with $\delta(M_p) < 20\%$ (314 of them, as of 2016 April 20), HAT-P-47b is the 4th lowest density, and HAT-P-48b is the 11th lowest density exoplanet. While the orbital solution for both planets is broadly consistent with circular orbits, it is possible that they are on slightly eccentric orbits, which could contribute to their large radii via tidal heating. Carrying out measurements of the occultations (secondary eclipses) of these planets could help in constraining their eccentricities.

We also plot the mass-density diagram, this time not limiting ourselves to $M_p < 0.3 M_J$, but considering *all transiting sub-stellar* objects with relative error on mass $< 20\%$ (Fig. 7). HAT-P-47b and HAT-P-48b clearly fall in a so-far unpopulated region of the parameter space: they are somewhat detached from the rest of the population in being light and very low density. Both objects fall close to, but below the approximate locus of Neptunian-to-Jovian class transition point of $\sim 0.4 M_J$ (Chen & Kipping 2016).

When plotting the mass vs. the semi-major axis of the planets ($M_p \sin i$ for non-transiting radial velocity detections), HAT-P-47b and HAT-P-48b fall in the “desert” between hot (small semi-major axis) Jupiters and hot super Earths (Fig. 8). This area of the parameter space has been coined the short-period Neptunian “desert”

TABLE 6

HIGH-PRECISION DIFFERENTIAL PHOTOMETRY OF HAT-P-48.

BJD ^a (2,400,000+)	Mag ^b	σ_{Mag}	Mag(orig) ^c	Filter
55574.58102	0.00063	0.00125	10.95120	<i>i</i>
55574.58164	-0.00182	0.00123	10.94760	<i>i</i>
55574.58244	-0.00110	0.00123	10.95170	<i>i</i>
55574.58307	0.00250	0.00122	10.95370	<i>i</i>
55574.58386	-0.00287	0.00122	10.94890	<i>i</i>
55574.58447	-0.00085	0.00121	10.95090	<i>i</i>
55574.58529	-0.00063	0.00122	10.95050	<i>i</i>
55574.58590	-0.00006	0.00122	10.95010	<i>i</i>
55574.58671	-0.00339	0.00122	10.94660	<i>i</i>
55574.58733	-0.00118	0.00122	10.94970	<i>i</i>

NOTE. — This table is available in a machine-readable form in the online journal. A portion is shown here for guidance regarding its form and content.

^a Barycentric Julian Date calculated directly from UTC, *without* correction for leap seconds.

^b The out-of-transit level has been subtracted. These magnitudes have been subjected to the EPD and TFA procedures, carried out simultaneously with the transit fit.

^c Raw magnitude values without application of the EPD and TFA procedures.

²⁰ <http://exoplanetarchive.ipac.caltech.edu/>

TABLE 7
ADOPTED STELLAR PARAMETERS FOR HAT-P-47–HAT-P-48 ASSUMING CIRCULAR ORBITS

Parameter	HAT-P-47 Value	HAT-P-48 Value	Source
Identifying Information			
R.A.	02 ^h 33 ^m 13.97s	02 ^h 57 ^m 53.03s	2MASS
Dec.	+30°21′37.8″	+30°37′32.5″	2MASS
GSC ID	GSC 2324-00031	GSC 2326-00214	GSC
2MASS ID	2MASS 02331396+3021377	2MASS 02575301+3037324	2MASS
Spectroscopic properties			
$T_{\text{eff}\star}$ (K)	6703 ± 50	5946 ± 50	SPC ^a
[Fe/H]	0.0 ± 0.08	0.02 ± 0.08	SPC
$v \sin i$ (km s ⁻¹)	14.1 ± 0.5	2.6 ± 0.5	SPC
γ_{RV} (km s ⁻¹)	2.70 ± 0.1	18.29 ± 0.1	TRES
Photometric properties			
V (mag)	10.694 ± 0.063	12.16 ± 0.11	TASS
I_C (mag)	10.084 ± 0.069	11.253 ± 0.071	TASS
J (mag)	9.713 ± 0.021	10.696 ± 0.023	2MASS
H (mag)	9.454 ± 0.022	10.340 ± 0.026	2MASS
K_s (mag)	9.404 ± 0.017	10.255 ± 0.021	2MASS
Derived properties			
M_\star (M_\odot)	1.387 ± 0.038	1.099 ± 0.041	YY+a/ R_\star +SPC ^b
R_\star (R_\odot)	1.515 ± 0.040	1.223 ± 0.046	YY+a/ R_\star +SPC
log g_\star (cgs)	4.22 ± 0.02	4.30 ± 0.03	YY+a/ R_\star +SPC
L_\star (L_\odot)	4.15 ± 0.27	1.67 ± 0.14	YY+a/ R_\star +SPC
M_V (mag)	3.17 ± 0.07	4.25 ± 0.10	YY+a/ R_\star +SPC
M_K (mag,ESO)	2.25 ± 0.06	2.81 ± 0.09	YY+a/ R_\star +SPC
Age (Gyr)	1.5 ± 0.3	4.7 ^{+1.3} _{-0.8}	YY+a/ R_\star +SPC
A_V (mag) ^c	0.414 ± 0.077	0.500 ± 0.110	YY+a/ R_\star +SPC
Distance (pc)	268 ± 7	305 ± 12	YY+a/ R_\star +SPC
log R'_{HK} ^d	-5.125 ± 0.015	-5.203 ± 0.029	Keck/HIRES

^a SPC = “Stellar Parameter Classification” method based on cross-correlating high-resolution spectra against synthetic templates (Buchhave et al. 2012). These parameters rely primarily on SPC, but have a small dependence also on the iterative analysis incorporating the isochrone search and global modeling of the data, as described in the text.

^b YY+a/ R_\star +SPC = Based on the YY isochrones (Yi et al. 2001), a/R_\star as a luminosity indicator, and the SPC results.

^c V band extinction determined by comparing the measured 2MASS and TASS photometry for the star to the expected magnitudes from the YY+a/ R_\star +SPC model for the star. We use the Cardelli et al. (1989) extinction law.

^d Chromospheric activity index defined in Noyes et al. (1984) determined from the Keck/HIRES spectra following Isaacson & Fischer (2010). In each case we give the average value and the standard deviation from the individual spectra.

TABLE 8
DERIVED STELLAR PARAMETERS FOR HAT-P-47–HAT-P-48 ALLOWING
ECCENTRIC ORBITS^a

Parameter	HAT-P-47 Value	HAT-P-48 Value	Source
M_\star (M_\odot)	1.402 ^{+0.099} _{-0.049}	1.083 ^{+0.087} _{-0.060}	YY+a/ R_\star +SPC
R_\star (R_\odot)	1.545 ^{+0.316} _{-0.117}	1.524 ± 0.270	YY+a/ R_\star +SPC
log g_\star (cgs)	4.20 ± 0.10	4.10 ± 0.13	YY+a/ R_\star +SPC
L_\star (L_\odot)	4.32 ^{+2.11} _{-0.65}	2.41 ^{+1.12} _{-0.68}	YY+a/ R_\star +SPC
M_V (mag)	3.13 ± 0.30	3.87 ± 0.38	YY+a/ R_\star +SPC
M_K (mag,ESO)	2.21 ± 0.30	2.37 ± 0.38	YY+a/ R_\star +SPC
Age (Gyr)	1.6 ^{+0.3} _{-0.6}	6.9 ± 1.3	YY+a/ R_\star +SPC
A_V (mag)	0.414 ± 0.079	0.419 ± 0.111	YY+a/ R_\star +SPC
Distance (pc)	273 ⁺⁵⁵ ₋₂₀	376 ± 67	YY+a/ R_\star +SPC

^a Quantities and abbreviations are as in Table 7, which gives our adopted values, determined assuming circular orbits. We do not list parameters that are independent of the eccentricity.

TABLE 9
ADOPTED ORBITAL AND PLANETARY PARAMETERS ASSUMING CIRCULAR ORBITS

Parameter	HAT-P-47b Value	HAT-P-48b Value
Light curve parameters		
P (days)	4.732182 ± 0.000013	4.408650 ± 0.000008
T_c (BJD) ^a	$2455661.63669 \pm 0.00041$	$2455839.21023 \pm 0.00029$
T_{14} (days) ^a	0.1287 ± 0.0015	0.1411 ± 0.0013
$T_{12} = T_{34}$ (days) ^a	0.0258 ± 0.0014	0.0165 ± 0.0013
a/R_*	8.73 ± 0.20	$9.53^{+0.36}_{-0.27}$
ζ/R_* ^b	19.05 ± 0.19	16.01 ± 0.08
R_p/R_*	0.0890 ± 0.0013	0.0951 ± 0.0016
b^2	$0.630^{+0.017}_{-0.017}$	$0.281^{+0.040}_{-0.057}$
$b \equiv a \cos i/R_*$	$0.794^{+0.010}_{-0.011}$	$0.530^{+0.036}_{-0.060}$
i (deg)	84.8 ± 0.2	$86.8^{+0.5}_{-0.3}$
Limb-darkening coefficients ^c		
c_1, i (linear term)	0.1592	0.2434
c_2, i (quadratic term)	0.3774	0.3424
c_1, r	0.2273	0.3246
c_2, r	0.3906	0.3445
RV parameters		
K (m s ⁻¹)	19.9 ± 3.8	19.6 ± 2.8
e	0 (fixed)	0 (fixed)
RV jitter Keck/HIRES (m s ⁻¹) ^d	22.0	20.5
RV jitter Subaru/HDS (m s ⁻¹) ^d	0.0	0.0
RV jitter NOT/FIES (m s ⁻¹) ^d	17.5
Planetary parameters		
M_p (M_J)	0.206 ± 0.039	0.168 ± 0.024
R_p (R_J)	1.313 ± 0.045	1.131 ± 0.054
$C(M_p, R_p)$ ^e	0.05	0.07
ρ_p (g cm ⁻³)	0.11 ± 0.02	$0.14^{+0.03}_{-0.02}$
$\log g_p$ (cgs)	$2.47^{+0.07}_{-0.11}$	2.51 ± 0.07
a (AU)	0.0615 ± 0.0006	0.0543 ± 0.0007
T_{eq} (K) ^f	1605 ± 22	1361 ± 25
Θ^g	0.014 ± 0.003	0.015 ± 0.002
$\langle F \rangle$ (10 ⁸ erg s ⁻¹ cm ⁻²) ^h	15.0 ± 0.8	7.75 ± 0.57

^a Reported times are in Barycentric Julian Date calculated directly from UTC, *without* correction for leap seconds. T_c : Reference epoch of mid transit that minimizes the correlation with the orbital period. T_{14} : total transit duration, time between first to last contact; $T_{12} = T_{34}$: ingress/egress time, time between first and second, or third and fourth contact.

^b Reciprocal of the half duration of the transit used as a jump parameter in our MCMC analysis in place of a/R_* . It is related to a/R_* by the expression $\zeta/R_* = a/R_*(2\pi(1 + e \sin \omega))/(P\sqrt{1 - b^2}\sqrt{1 - e^2})$ (Bakos et al. 2010).

^c Values for a quadratic law, adopted from the tabulations by Claret (2004) according to the spectroscopic (SPC) parameters listed in Table 7.

^d Error term, either astrophysical or instrumental in origin, added in quadrature to the formal RV errors for the listed instrument such that χ^2 per degree of freedom is unity. For both HAT-P-47 and HAT-P-48 we did not add jitter to the Subaru/HDS RV errors because the formal errors for these observations exceeded the scatter in the RV residuals.

^e Correlation coefficient between the planetary mass M_p and radius R_p .

^f Planet equilibrium temperature averaged over the orbit, calculated assuming a Bond albedo of zero, and that flux is reradiated from the full planet surface.

^g The Safronov number is given by $\Theta = \frac{1}{2}(V_{\text{esc}}/V_{\text{orb}})^2 = (a/R_p)(M_p/M_*)$ (see Hansen & Barman 2007).

^h Incoming flux per unit surface area, averaged over the orbit.

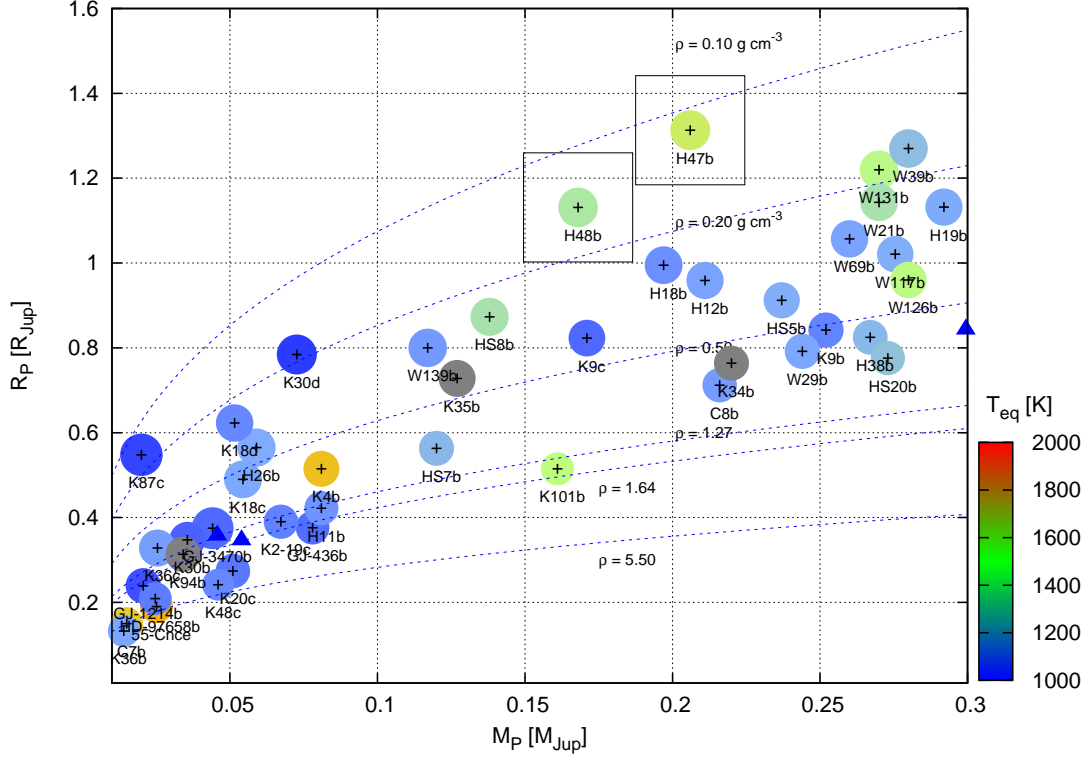


FIG. 6.— Mass-radius diagram of sub-Saturn mass TEPs ($M_p < 0.3M_J$), where the relative error of the mass determination is $\delta(M_p) < 20\%$. HAT-P-47b and HAT-P-48b are highlighted by large boxes (these are not error-bars). The color-bar indicates equilibrium temperature (with a palette of R,G,B = 2000, 1500, 1000 K). Solar System planets are indicated by blue triangles. Both HAT-P-47b and HAT-P-48b stand out by their very low density.

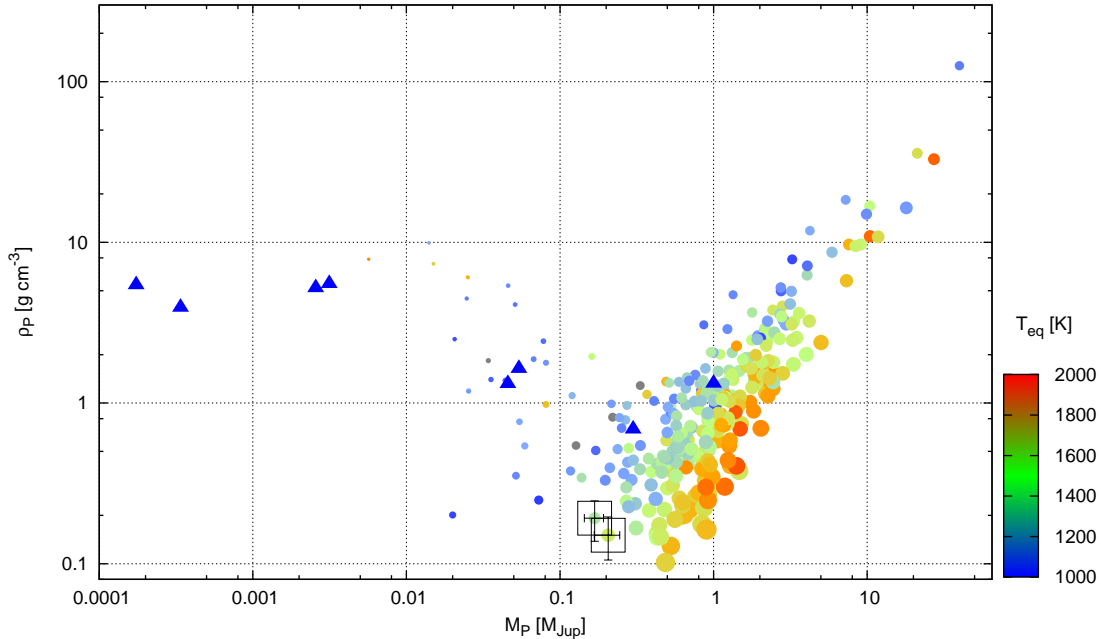


FIG. 7.— Planetary mean density vs. mass for TEPs with mass measured at $\delta(M_p) < 20\%$ precision. HAT-P-47b and HAT-P-48b are highlighted by large boxes. The size of the points scales with planetary radius, while the color indicates equilibrium temperature (as in Fig. 6). HAT-P-47b and HAT-P-48b fall in a so-far unpopulated region of the parameter space; they are the lowest density sub-Saturn objects. Solar system planets are marked with blue triangles.

TABLE 10
ORBITAL AND PLANETARY PARAMETERS ALLOWING ECCENTRIC
ORBITS^a

Parameter	HAT-P-47b Value	HAT-P-48b Value
Light curve parameters		
a/R_*	$8.57^{+0.68}_{-1.15}$	$7.61^{+1.37}_{-1.01}$
ζ/R_*	19.05 ± 0.19	16.07 ± 0.11
i (deg)	$84.6^{+0.7}_{-2.5}$	$84.9^{+1.5}_{-2.5}$
RV parameters		
K (m s^{-1})	20.0 ± 4.5	20.9 ± 2.8
$\sqrt{e} \cos \omega$	-0.116 ± 0.210	0.014 ± 0.155
$\sqrt{e} \sin \omega$	0.058 ± 0.251	$0.464^{+0.124}_{-0.294}$
$e \cos \omega$	$-0.030^{+0.067}_{-0.113}$	0.004 ± 0.076
$e \sin \omega$	$0.010^{+0.149}_{-0.071}$	0.227 ± 0.145
e	0.101 ± 0.101	0.242 ± 0.136
ω (deg)	161 ± 85	90 ± 60
Secondary eclipse parameters		
T_s (BJD)	2455692.30 ± 0.28	2455819.38 ± 0.22
$T_{s,14}$	0.128 ± 0.021	0.166 ± 0.030
$T_{s,12}$	0.027 ± 0.028	0.039 ± 0.040
Planetary parameters		
M_p (M_J)	0.206 ± 0.048	0.173 ± 0.023
R_p (R_J)	$1.342^{+0.274}_{-0.109}$	1.407 ± 0.253
$C(M_p, R_p)$	0.22	0.29
ρ_p (g cm^{-3})	0.10 ± 0.04	$0.08^{+0.06}_{-0.03}$
$\log g_p$ (cgs)	$2.44^{+0.11}_{-0.17}$	2.33 ± 0.15
a (AU)	$0.0617^{+0.0014}_{-0.0007}$	$0.0540^{+0.0014}_{-0.0010}$
T_{eq} (K)	1621^{+145}_{-60}	1508 ± 131
Θ	0.013 ± 0.003	$0.012^{+0.003}_{-0.002}$
$\langle F \rangle$ ($10^8 \text{ erg s}^{-1} \text{ cm}^{-2}$)	$15.6^{+7.1}_{-2.1}$	$11.7^{+5.4}_{-3.2}$

^a Quantities and definitions are as in Table 9, which gives our adopted values, determined assuming circular orbits. Here we do not list parameters that are effectively independent of the eccentricity.

(Szabó & Kiss 2011; Mazeh et al. 2016, and references therein). A similar desert has been identified for planets around M-dwarf host stars (Gaidos et al. 2016). The desert is especially pronounced for $P < 5$ days, so with their respective periods of 4.7322 d and 4.4087 d, both objects are on the “edge” of the desert. One possible explanation for the lack of planets in this domain is that small gaseous objects can not survive the proximity of the star, unlike large gaseous objects (hot Jupiters), or small, dense, rocky planets.

Measuring the Rossiter-McLaughlin effect (R-M; Queloz et al. 2000; Winn et al. 2005) for HAT-P-47b and HAT-P-48b would provide an interesting test of the hypothesis that the obliquities of close-in giant planets were initially nearly random, and that subsequent star-planet tidal interactions act to reduce the obliquities (e.g., Albrecht et al. 2012). With effective temperatures of 6703 ± 50 K and 5946 ± 50 K, HAT-P-47 and HAT-P-48 are expected to have radiative and convective envelopes, respectively. While most close-in transiting planets around stars with convective envelopes have been found to be on low-obliquity orbits, those around radiative envelope stars have been found to have a wide range of obliquities (Winn et al. 2010). If this difference is the result of a dependence on stellar mass of the dominant planet migration pathway, then we might expect HAT-P-48b to be on a low-obliquity orbit while HAT-P-47b would likely be misaligned. If, however, the low obliquity orbits are the result of tidal interactions, then based on Figure 24 of Albrecht et al. (2012) we would expect both HAT-P-47b and HAT-P-48b to be misaligned. This is due to the low planet masses, and the resulting long tidal interaction timescales (Equations 2 and 3 from Albrecht et al. 2012, which in turn are taken from Zahn 1977), even for HAT-P-48 with its convective envelope. HAT-P-48b is at an interesting mass where we expect the tidal interaction to be comparable to WASP-8b, a misaligned planet around a convective envelope star which has a mass of $2.2 M_J$, but a long orbital period of 8.16 days (Queloz et al. 2010). Measuring the R-M effect is feasible for both systems. Assuming aligned orbits, we expect HAT-P-47b to have an R-M amplitude of 68 m s^{-1} , while HAT-P-48b would have an amplitude of 20 m s^{-1} . Which, given the magnitudes and RV jitter, should be detectable from single transits with Keck/HIRES.

Finally, we calculate the expected transmission spectroscopy signature for both planets as $\delta = 5 \times 2R_p H / R_*^2$ (Perryman et al. 2014), where H is the scale height of the atmosphere. In calculating the latter quantity, we assume the molecular weight of pure molecular hydrogen, and the equilibrium temperature and surface gravity of the planet as determined from our analysis (Tab. 9). Once δ is known, we then calculate the K-band flux of the star, and multiply by δ , to come up with an approximate measure of the transmission signal. This quantity does not take into account the detailed (expected) spectrum of the planetary atmosphere, but is an order of magnitude estimate of the signature. The results are plotted in Fig. 9 for planets with $M_p \leq 0.25 M_J$. For both HAT-P-47b and HAT-P-48b the expected transmission signature is amongst the largest for sub-Saturn objects, making these new discoveries especially valuable.

Acknowledgements— HATNet operations have been funded by NASA grants NNG04GN74G, NNX08AF23G, NNX13AJ15G and SAO IR&D grants. We acknowledge partial support also from the Kepler Mission under NASA Cooperative Agreement NCC2-1390 (D.W.L., PI). This research has made use of Keck telescope time granted through NOAO (A284Hr, A245Hr) and NASA (N108Hr, N154Hr, N130Hr). Based in part on data collected at Subaru Telescope (program o11170), which is operated by the National Astronomical Observatory of Japan. This paper presents observations made with the Nordic Optical Telescope, operated on the island of La Palma jointly by Denmark, Finland, Iceland, Norway, and Sweden, in the Spanish Observatorio del Roque de los Muchachos of the Instituto de Astrofísica de Canarias. This paper uses observations obtained with facilities of the Las Cumbres Observatory Global Telescope. The Byrne Observatory at Sedgwick (BOS) is operated by the Las Cumbres Observatory Global Telescope Network and is located at the Sedgwick Reserve, a part of the University of California Natural Reserve System. B.J.F. notes that this material is based upon work supported by the National Science Foundation Graduate Research Fellowship under grant No. 2014184874. Data presented in this paper are based on observations obtained at the HAT station at the Submillimeter Array of SAO, and the HAT station at the Fred Lawrence Whipple Observatory of SAO. We wish to thank J. Johnson his contribution to the Keck/HIRES radial velocity observations. The authors wish to recognize and acknowledge the very significant cultural role and reverence that the summit of Mauna Kea has always had within the indigenous Hawaiian community. This research has made use of the NASA Exoplanet Archive, which is operated by the California Institute of Technology, under contract with the National Aeronautics and Space Administration under the Exoplanet Exploration Program.

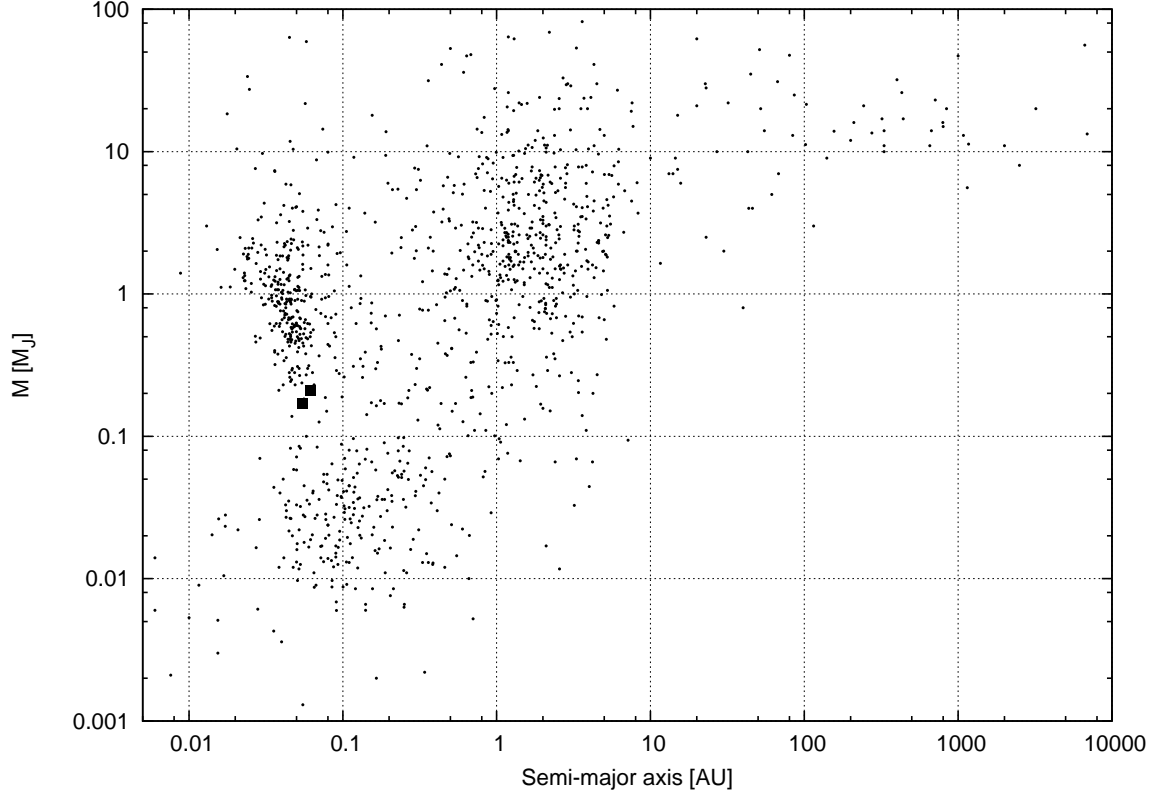


FIG. 8.— Mass vs. semi-major axis of exoplanets from exoplanet.eu^a. For non-transiting systems, $M_p \sin i$ is used instead of the true mass. HAT-P-47b and HAT-P-48b are indicated with black filled boxes, both falling in the sparse region between hot Jupiters and hot super-Earths.

^a<http://exoplanetarchive.ipac.caltech.edu/>

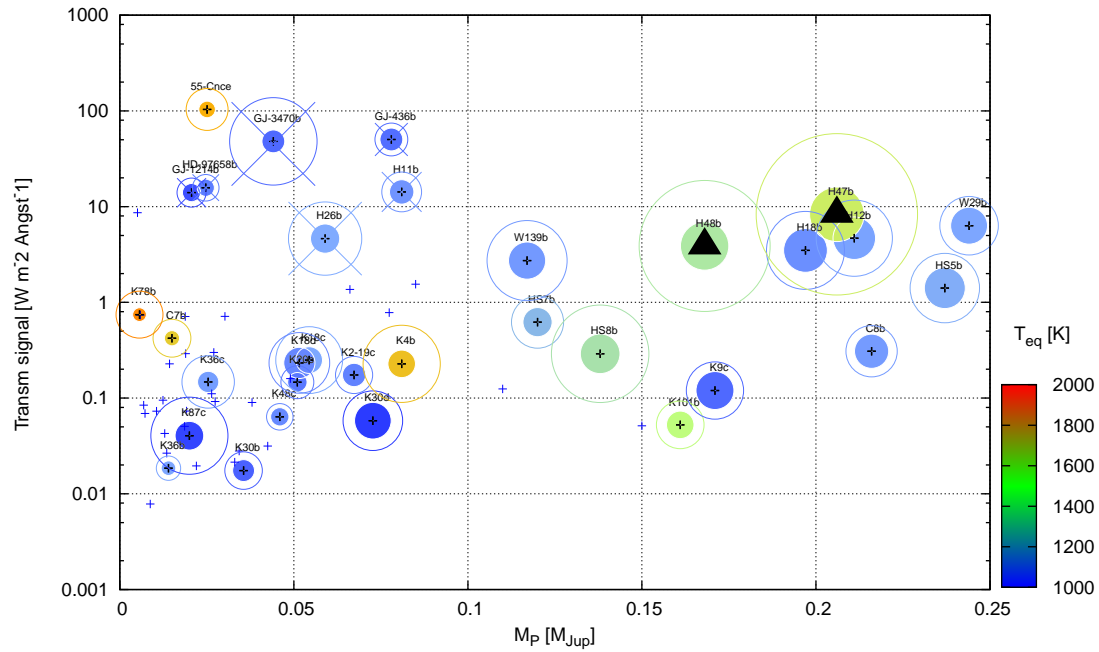


FIG. 9.— Approximate detectability of a planet's atmosphere in transmission, as a function of planetary mass for planets with $M_p \leq 0.25 M_{\text{J}}$. The size of the filled circles scales with the radius of the planet (arbitrary scale), and the radius of the open circles scales with the scale height of the atmosphere. Small plus symbols denote planets with uncertain mass or radius measurements (error >20%). The color-bar is the same as for Fig. 7. Transmission spectroscopy has been carried out for planets with diagonal crosses. HAT-P-47b and HAT-P-48b are marked with black triangles. Abbreviations are: K: Kepler, H: HAT, HS: HATSouth, C: Corot, W: WASP.

REFERENCES

- Albrecht, S., Winn, J. N., Johnson, J. A., et al. 2012, *ApJ*, 757, 18
- Anderson, D. R., Collier Cameron, A., Gillon, M., et al. 2012, *MNRAS*, 422, 1988
- Bakos, G., Noyes, R. W., Kovács, G., et al. 2004, *PASP*, 116, 266
- Bakos, G. Á., Torres, G., Pál, A., et al. 2010, *ApJ*, 710, 1724
- Brown, T. M., Baliber, N., Bianco, F. B., et al. 2013, *PASP*, 125, 1031
- Buchhave, L. A., Bakos, G. Á., Hartman, J. D., et al. 2010, *ApJ*, 720, 1118
- Buchhave, L. A., Latham, D. W., Johansen, A., et al. 2012, *Nature*, 486, 375
- Burrows, A., Hubeny, I., Budaj, J., & Hubbard, W. B. 2007, *ApJ*, 661, 502
- Butler, R. P., Marcy, G. W., Williams, E., et al. 1996, *PASP*, 108, 500
- Cardelli, J. A., Clayton, G. C., & Mathis, J. S. 1989, *ApJ*, 345, 245
- Chen, J., & Kipping, D. M. 2016, *ArXiv e-prints*
- Claret, A. 2004, *A&A*, 428, 1001
- Djupvik, A. A., & Andersen, J. 2010, in *Highlights of Spanish Astrophysics V*, ed. J. M. Diego, L. J. Goicoechea, J. I. González-Serrano, & J. Gorgas, 211
- Droege, T. F., Richmond, M. W., Sallman, M. P., & Creager, R. P. 2006, *PASP*, 118, 1666
- Fűresz, G. 2008, PhD thesis, Univ. of Szeged, Hungary
- Gaidos, E., Mann, A. W., Kraus, A. L., & Ireland, M. 2016, *MNRAS*, 457, 2877
- Girardi, L., Bertelli, G., Bressan, A., et al. 2002, *A&A*, 391, 195
- Hansen, B. M. S., & Barman, T. 2007, *ApJ*, 671, 861
- Hartman, J. D., Bakos, G. Á., Torres, G., et al. 2011, *ApJ*, 742, 59
- Hartman, J. D., Bakos, G. Á., Béky, B., et al. 2012, *AJ*, 144, 139
- Hébrard, G., Collier Cameron, A., Brown, D. J. A., et al. 2013, *A&A*, 549, A134
- Huang, C. X., Hartman, J. D., Bakos, G. Á., et al. 2015, *AJ*, 150, 85
- Isaacson, H., & Fischer, D. 2010, *ApJ*, 725, 875
- Kovács, G., Zucker, S., & Mazeh, T. 2002, *A&A*, 391, 369
- Kovács, G., Bakos, G. Á., Hartman, J. D., et al. 2010, *ApJ*, 724, 866
- Latham, D. W., Bakos, G. Á., Torres, G., et al. 2009, *ApJ*, 704, 1107
- Masuda, K. 2014, *ApJ*, 783, 53
- Mazeh, T., Holczer, T., & Faigler, S. 2016, *A&A*, 589, A75
- Noguchi, K., Aoki, W., Kawanamoto, S., et al. 2002, *PASJ*, 54, 855
- Noyes, R. W., Hartmann, L. W., Baliunas, S. L., Duncan, D. K., & Vaughan, A. H. 1984, *ApJ*, 279, 763
- Perryman, M., Hartman, J., Bakos, G. Á., & Lindegren, L. 2014, *ApJ*, 797, 14
- Queloz, D., Eggenberger, A., Mayor, M., et al. 2000, *A&A*, 359, L13
- Queloz, D., Anderson, D. R., Collier Cameron, A., et al. 2010, *A&A*, 517, L1
- Quinn, S. N., Bakos, G. Á., Hartman, J., et al. 2012, *ApJ*, 745, 90
- Sato, B., Kambe, E., Takeda, Y., Izumiura, H., & Ando, H. 2002, *PASJ*, 54, 873
- Sato, B., Omiya, M., Harakawa, H., et al. 2012, *PASJ*, 64
- Smalley, B., Anderson, D. R., Collier-Cameron, A., et al. 2012, *A&A*, 547, A61
- Spiegel, D. S., & Burrows, A. 2013, *ApJ*, 772, 76
- Szabó, G. M., & Kiss, L. L. 2011, *ApJ*, 727, L44
- Torres, G., Bakos, G. Á., Kovács, G., et al. 2007, *ApJ*, 666, L121
- Vogt, S. S., Allen, S. L., Bigelow, B. C., et al. 1994, in *Society of Photo-Optical Instrumentation Engineers (SPIE) Conference Series*, Vol. 2198, Society of Photo-Optical Instrumentation Engineers (SPIE) Conference Series, ed. D. L. Crawford & E. R. Craine, 362
- Winn, J. N., Noyes, R. W., Holman, M. J., et al. 2005, *ApJ*, 631, 1215
- Winn, J. N., Johnson, J. A., Howard, A. W., et al. 2010, *ApJ*, 718, 575
- Yi, S., Demarque, P., Kim, Y.-C., et al. 2001, *ApJS*, 136, 417
- Zahn, J.-P. 1977, *A&A*, 57, 383